nature geoscience

LETTERS

PUBLISHED ONLINE: 15 SEPTEMBER 2013 | DOI: 10.1038/NGEO1933

Fine-scale segmentation of the crustal magma reservoir beneath the East Pacific Rise

Suzanne M. Carbotte[1]*, Milena Marjanović[1], Helene Carton[1], John C. Mutter[1], Juan Pablo Canales[2], Mladen R. Nedimović[1,3], Shuoshuo Han[1] and Michael R. Perfit[4]

The global mid-ocean ridge is segmented in its seafloor morphology and magmatic systems, but the origin of and relationships between this tectonic and magmatic segmentation are poorly understood[1–5]. At fast-spreading ridges, tectonic segmentation is observed on a fine scale[2,4,6–8], but it is unclear whether this partitioning also occurs in the magmatic system. Fine-scale tectonic segmentation could have a deep origin, arising from the distribution of upwelling mantle melt, or a shallow origin, linked to offset intruding dikes from long, more continuous crustal reservoirs[2,9]. Here we use seismic reflection data from the fast-spreading East Pacific Rise, between 8° 20′ N and 10° 10′ N, which includes a unique area where two documented volcanic eruptions have occurred[10–15], to image the crustal magma bodies in high resolution. We find that the magma reservoirs form 5- to 15-km-long segments that coincide with the fine-scale tectonic segmentation at the seafloor and that three lens segments fed the recent eruptions. Transitions in composition, volume and morphology of erupted lavas coincide with disruptions in the lens that define magmatic segments. We conclude that eruptions at the East Pacific Rise are associated with the vertical ascent of magma from lenses that are mostly physically isolated, leading to the eruption of distinct lavas at the surface that coincide with fine-scale tectonic segmentation.

Most volcanic and hydrothermal activity along the fast-spreading northern East Pacific Rise (EPR) occurs within a small (<20 m high, <500 m wide) depression known as the axial summit trough (AST) or along axis-centred ridges of pillow lavas[6–8,16]. These seafloor structures encompass the zone of primary eruptive fissures for the eruptions and dyke intrusions that build the upper crust and are readily identified in high-resolution sonar data from the EPR axis[2,4,6–8,16] (Fig. 1). The magma source reservoir for these volcanic events is a thin (tens of metres) lens of fully to partially molten magma, located in the mid-to-upper crust and roughly centred beneath, but wider (0.5–4 km) than the seafloor eruptive fissure zone above (for example, ref. 17). Seismic tomography data indicate that this thin magma lens is located above a broader, 4–6-km-wide, region extending into the lower crust that is thought to be composed of a crystal mush of hot rock and distributed melt[9].

New multi-channel seismic (MCS) reflection data are used here to characterize the present-day magma lens beneath a zone of modern volcanic eruptions at ∼9° 50′ N and adjoining EPR from 8° 20 to 10° 10′ N (Methods). From a series of lines shot along the ridge axis, the seismic line closest to the innermost axial zone (centre of the AST or axial pillow ridge) is identified (Fig. 1 and Supplementary Figs S1 and S2) and a composite profile is constructed (Fig. 2). The composite profile provides a cross-sectional view of the magma lens at the location where modern hydrothermal venting, historic eruptions and eruptive fissures are narrowly focused. The seismic data reveal an axial magma lens (AML) reflection beneath ∼85% of the innermost axial zone that varies in depth over short spatial scales about an average depth of ∼1.6 km. However, the AML reflection is not a continuous event. Numerous disruptions in the AML are evident (Fig. 1b), including breaks with steps in AML two-way travel time (TWTT), edge diffractions in stack sections, or regions of two AML reflections that overlap in depth. Five of these discontinuities are resolved in MCS data acquired for three-dimensional (3D) imaging from ∼9° 37′ to 40′ N and 9° 42′ to 57′ N and correspond with offset and overlapping melt zones in plan view[18] (Supplementary Fig. S2a). Using the nature of lens discontinuities interpreted from the 3D volumes as a guide, minima criteria are defined (Methods) and AML disruptions are identified along the full length of the profile (Fig. 2). AML disruption zones, with lateral along-axis extents of up to 1.5 km, define a magma lens that is partitioned into segments 5–15 km long. AML depth varies within individual lens segments and many AML disruptions lie at local depth maxima (Fig. 2 and Supplementary Notes and Fig. S3).

Previously collected seismic reflection data from the region showed separate magma lens bodies beneath both limbs of the large overlapping spreading centre (OSC) at 9° 03′ N (ref. 19), as well as evidence for segmentation of the AML coincident with smaller offsets of the axis at 9° 37′ N and 9° 19–21′ N (ref. 17). These smaller offsets are classified as third-order tectonic discontinuities on the basis of offset length (0.5 and 1 km) and evidence for a ridge-flank trace indicating persistence for hundreds of thousands of years (refs 2–4). Our modern seismic data, acquired with a high-quality tuned seismic source and well located along the axial zone, indicate disruptions in the AML at both of these axial discontinuities as well as at all other identified third-order offsets (Fig. 2). Furthermore, the new data show that the smaller-scale or fourth-order offsets of the eruptive fissure zone[2,6] also coincide with segmentation of the underlying magma lens. These fourth-order discontinuities are defined by small lateral steps (50–500 m) in the AST or axial pillow ridges, or changes in width or trend of these structures[2,6,8]. All of these discontinuities are associated with small bends or steps in the broader (∼4 km wide) axial high and/or local pinches in the cross-axis morphology, indicating longevity for perhaps thousands of years[2,4,8], in spite of the small offset of the axial zone (Fig. 1 and Supplementary Figs S1 and S2). At most seafloor discontinuities (75%), a magma lens disruption zone is identified within the subsurface (within 1 km;

[1]Lamont-Doherty Earth Observatory of Columbia University, Palisades, New York 10964, USA, [2]Woods Hole Oceanographic Institution, Woods Hole, Massachusetts 02543, USA, [3]Dalhousie University, Department of Earth Sciences, Halifax, Nova Scotia B3H 4J1, Canada, [4]University of Florida, Department of Geological Sciences, Gainseville, Florida 32611, USA. *e-mail: carbotte@ldeo.columbia.edu

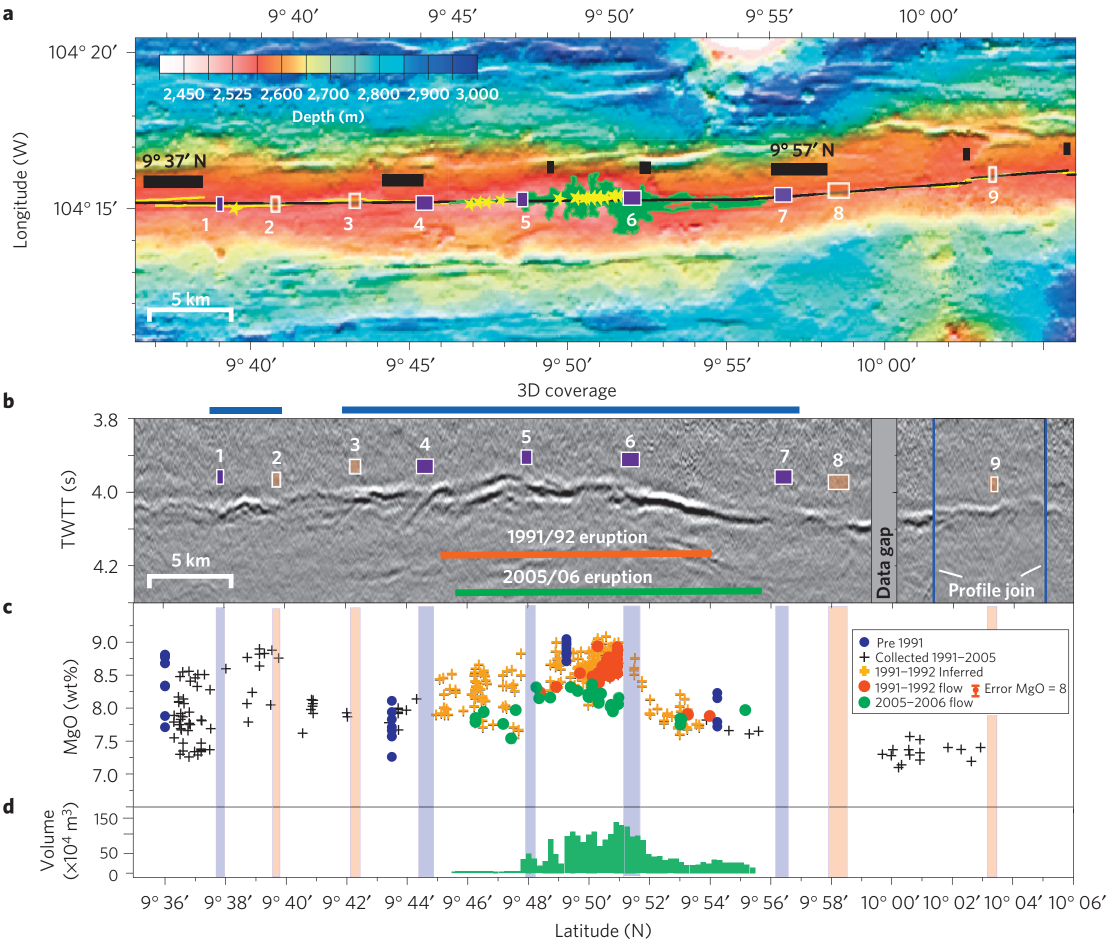

Figure 1 | Segmentation in seafloor structure, AML, lava geochemistry and eruption volume along the EPR 9° 35′–10° 06′ N. a, Bathymetry showing location of axial eruptive zone (yellow line, from refs 8,12,16) and composite axial seismic profile (black). Black rectangles: third- (labelled) and fourth-order tectonic discontinuities. Yellow stars: hydrothermal vents[30]; green region: 2005–2006 lava flow[12]. **b**, Composite axial seismic reflection section (stacked) showing magma lens reflection and interpreted disruptions. TWTT, two-way travel time. Numbered rectangles in **a**,**b** indicate magma lens disruptions identified from seismic data (purple, data from 3D seismic volume). **c**, MgO composition of seafloor lavas located within 500 m of the axis (see Methods) colour-coded for eruption period. Microprobe analytic errors on natural glasses are ±1% of measured values and are indicated for MgO = 8.0 wt%. **d**, Volume of erupted 2005–2006 lavas[12] (Methods). Vertical bars (translucent purple and orange) mark magma lens disruptions from **a**,**b**.

Figs 1 and 2). From these relationships, we conclude that the fine-scale segmentation of the seafloor eruptive fissure zone is inherited from partitioning in the magma reservoir ~1.6 km below. Previous suggestions that fourth-order segmentation reflects shallow level processes associated with dyke intrusion from continuous magma reservoirs[1,2,6] can be ruled out.

Fine-scale segmentation in the chemistry of young seafloor lavas has long been recognized although the origin of this segmentation is not well understood[1]. A variety of factors may contribute to along-axis chemical diversity including magma evolution within crustal reservoirs, differences in mantle source composition and/or melt extraction within the mantle. These processes are expected to vary both spatially and temporally, but distinguishing among them is complicated by the limited age information available for seafloor lavas and the sparse sampling of most ridge areas. The EPR from ~9° N to the Clipperton transform fault is the most densely and frequently sampled portion of the global mid-ocean ridge. Major element compositions of axial lavas sampled in previous studies[1,3,13,14,20] (Methods) and known or assumed to have erupted in the past few hundred years reveal the presence of lavas of comparatively homogeneous composition separated by narrow regions of compositional transition/overlap (Fig. 1c). Regions of mostly uniform lava composition coincide well with the magma lens segmentation mapped from the seismic data, with distinct lava chemistry above most lens segments. Where dense sampling spans magma lens discontinuities, compositional transitions and AML discontinuities are co-located within ≤1 km.

The two documented volcanic eruptions in this region occurred in 1991–1992 (ref. 10) and 2005–2006 (refs 11,12,15), and in roughly the same location with erupted lavas extending for 16–18 km along the ridge axis[10,12] (Fig. 1). Glass MgO concentrations, which are a proxy for lava temperatures, are highest above the 9° 48–9° 51.5′ N magma lens segment, coincident with the central eruption source region for both eruptions[10,13]. Although the 2005–2006 lavas are slightly more evolved (lower MgO) than earlier lavas, spatial variations in lava geochemistry observed in the 1991–1992 lavas are preserved through the younger eruption (Fig. 1c and Supplementary Fig. S4) with more fractionated lavas erupted south of 9° 48′ N and north of 9° 51.5′ N (ref. 13). Geochemical data further indicate that northern lavas may have experienced shallower fractionation histories on average than lavas from the central region and for both eruptions, Zr/Y ratios are slightly elevated suggesting some differences in parental magmas[13]. We conclude that the three compositional zones erupted in both the

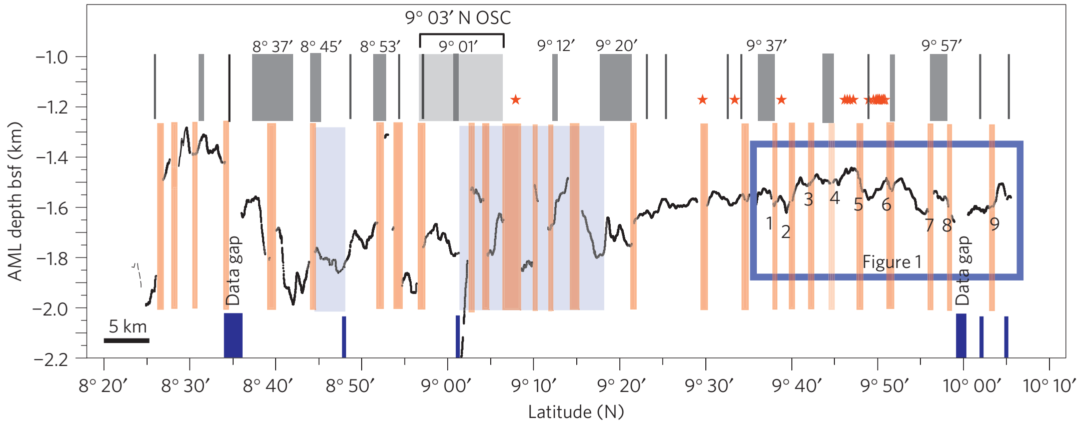

Figure 2 | Comparison of magma lens and bathymetric segmentation along the EPR 8° 20′–10° 10′ N. Depth below sea floor to AML reflection (black line) identified from seismic data (Methods and Supplementary Notes). Vertical orange bars indicate magma lens disruptions beneath the axis; the translucent purple shaded zones show areas where the seismic profile is >300 m from the axial zone, and/or the modern axis is difficult to identify and axial disruptions are poorly constrained. Grey lines/bars indicate bathymetric discontinuities (modified from ref. 8); 9° 03′ N OSC and third-order discontinuities are labelled. Short blue bars indicate data gaps and locations of joins between seismic lines of composite axial profile. Red stars indicate hydrothermal vents[30]. Bsf, below sea floor.

2005–2006 and earlier eruptions were fed from the three lens segments that underlie the present eruption zone. Furthermore, the preservation of compositional gradients through two eruptions, with more evolved compositions erupted in 2005–2006 relative to 1991–1992 and distinct parental melts inferred for northern lavas, indicates limited chemical mixing consistent with physical isolation of magma within adjacent lens segments.

Mapping of the 2005–2006 lava flow reveals three primary zones in lava morphology and erupted volume[12,21] with transitions also coincident with AML disruptions (Fig. 1d). Small eruptive volumes, entirely confined to the AST, are found above the southern lens segment. The largest eruptive volumes are mapped above the central segment where lavas extend to 2 km from the AST, with lower flow distances and mapped volumes above the northern segment. Differences in lava morphology have been attributed to variable lava effusion rates[21] and indicate different eruption conditions for the three lens segments.

These observations have significant implications for the mode of magma transport during dyke intrusion, a fundamental aspect of crustal formation about which little is known at fast-spreading ridges. Lateral magma transport at the EPR has been invoked to explain along-axis gradients in ridge properties including progressive deepening of the sea floor towards many ridge-axis discontinuities and the distinctive geometry of OSCs (for example, refs 2,4). Other indicators of lateral transport include magma flow markers and geochemical analyses of upper crustal exposures at Pito and Hess Deep, which require some component of horizontal magma transport in the dyke section[22,23]. However, our observations of distinct compositional and morphological segments in axial lavas from single eruptions coincident with segmentation of the underlying magma lens indicate that magma transport was predominantly vertical during these recent EPR eruptions (Fig. 3). Vertical magma transport has also been inferred along the southern EPR (ref. 24) where compositional boundaries in seafloor lavas of similar age are collocated with a discontinuity in the bathymetric axis at ~17° 29′ S and a possible discontinuity in the underlying AML. If vertical magma ascent from the finely segmented magma reservoir inferred from our seismic data is the primary mode of magma transport at the EPR, an upper crust composed of small-scale accretionary units[2] is expected. Each unit will have distinct geochemical characteristics, physical dimensions and eruptive histories determined by the evolution of the chemical and physical properties of the underlying magma lens segment in response to ongoing magma replenishment and episodic withdrawal.

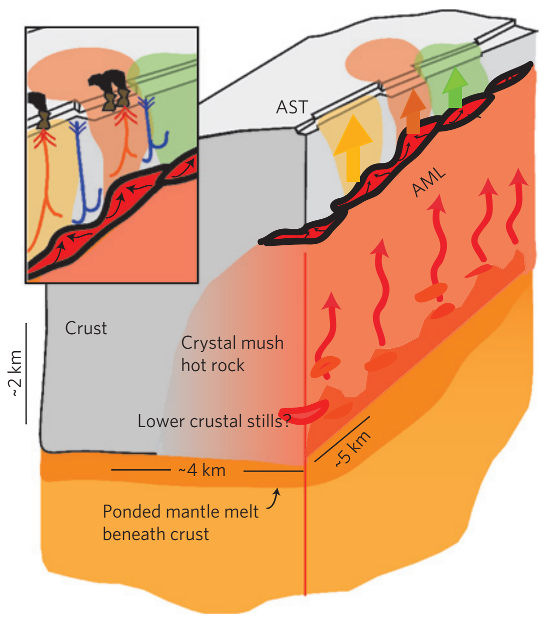

Figure 3 | Schematic representation of EPR magmatic system and 2005–2006 eruption. Segmented magma lens (red) sits atop zone of crystal mush (for example, ref. 9) and possible lower crustal sills[25] (light red). Mantle melts accumulate beneath crust[5,9] (orange). During dyking, compositionally distinct magmas intrude primarily vertically (broad arrows) from AML segments. Steps in AST coincide with AML segment boundaries. Possible factors contributing to AML segmentation include lower crustal melt focusing (red arrows), intrusions/eruptions and melt accumulation within the AML (black arrows), and (inset) variable cooling of AML through hydrothermal circulation. Inset: Arrows show hypothetical fluid downflow (blue) at seafloor discontinuities and upflow (red) beneath hydrothermal vents[29].

With magma present in the mid-crust beneath most of the ridge axis, why does it segregate into a series of 5–15 km elongate magma lens segments rather than form a continuous reservoir?

Both deep and shallow level processes are likely to contribute (Fig. 3). Focused melt transport may occur within the lower crust and shallow mantle through processes of melt channel formation or dyke intrusion from deep sills[25,26] forming punctuated sites of magma lens replenishment. Magma withdrawal associated with dyke intrusion and eruptions[27], and thermal erosion, stoping and crustal assimilation at the AML roof[28], are also likely to contribute to lens segmentation. Hydrothermal circulation above the magma lens may play an important role with local deepening and enhanced crystallinity within the AML predicted at sites of hydrothermal recharge[29]. The topography of the lens itself may play a key role in maintaining segmentation as buoyant melt migrates up-dip[19] and accumulates preferentially at local shoals. Our observations that many AML segments exhibit a convex shape in cross-section, and lens disruptions along the ridge axis often coincide with local depth maxima in the AML, are suggestive of this (Fig. 2 and Supplementary Notes).

Strong feedbacks are expected between hydrothermal cooling from above, dyke intrusion and eruption, and magma resupply from below[2,6]. These close linkages are evident in the relationships between hydrothermal vents, eruption history and AML structure within our study area. Most high-temperature vents in the region are located from 9° 46′ to 51′ N (refs 6,30) where both documented eruptions occurred. Here, the sea floor and AML shoal (Fig. 1 and Supplementary Fig. S3), and locally enhanced magma supply is inferred[2]. High-temperature vents form two clusters[6,30], centred above two of the three erupting lens segments and separated by a hydrothermal gap that spans the AML discontinuity and depth maxima at ∼9° 48′ N (Figs 1, 2). Differences in the chemistry and temporal evolution of vent fluids from these two clusters are documented[30] indicating distinct hydrothermal cells above the two lens segments, consistent with a closely coupled tectonic–magmatic–hydrothermal system.

Methods

Seismic reflection data acquisition and processing. Seismic reflection data were acquired during RV *Langseth* expedition MGL0812 and included 1–3 parallel lines shot along the EPR axis from 8° 20 to 10° 10′ N as well as a suite of lines shot perpendicular to the ridge for 3D imaging (Supplementary Fig. S1). Two 3,300-cubic-inch broadband source arrays were used in flip-flop mode with a 37.5 m shot interval. Data were recorded on four 6-km-long, 468-channel streamers with a 12.5 m receiver group spacing and a sampling interval of 2 ms. The recorded signal has a bandwidth ranging from ∼2 to 100 Hz with a dominant frequency of 10–30 Hz.

Reflection data used here were processed assuming a 2D geometry using recorded signals from one streamer and combining shots from both air-gun arrays providing a common midpoint fold of 78 and common midpoint spacing of 6.25 m. The pre-stack processing sequence includes merge of shot and navigation data, geometry definition, band-pass filter (2–7–100–125 Hz), trace edit, amplitude correction for spherical divergence and $f-k$ filter, surface-consistent amplitude correction, velocity analysis and normal move-out correction. The data are stacked for AML and sea floor using all traces to source–receiver offsets of 3 km and for the layer 2A horizon using traces from 1,500 to 3,000 m. The post-stack processing sequence includes sea floor and primary multiple mute to reduce migration noise, Kirchhoff time migration, and merge of layer 2A and AML sections. All processing is conducted using Paradigm's processing suite Focus.

From migrated sections, TWTTs to the AML reflection and the seismic layer 2A horizon are digitized using a guided digitizer tool and smoothed with a median filter (Supplementary Fig. S3). Estimated picking errors for all events are ±0.008 s. Seismic horizons are converted to depth assuming constant velocities of 2.26 km s^{-1} for layer 2A and 5.5 km s^{-1} for layer 2B. Stacking errors of ±0.016 s for layer 2A and ±0.008 s for the AML/seafloor events are estimated from the range of constant velocity stacks that optimally stack each event. Combined stacking and picking errors are ±0.018 s for the base of layer 2A and ±0.011 s for the AML, equivalent to depth uncertainties of ±20 m and ±35 m respectively for these events. See Supplementary Notes for further discussion of limitations in interpretation of AML structure from the 2D sections.

Identification of magma lens discontinuities. Within the region of 3D MCS coverage, disruptions in the axis-centred image of the AML are interpreted using the 3D data set and correspond with broad zones of overlapping and offset melt lenses (Supplementary Figs S1 and S2). Beyond this area, discontinuities in the AML event are identified where at minimum two of the following criteria are met: break in AML continuity with abrupt step in TWTT of >30 ms; gap in AML event of >400 m; edge diffraction in the stacked section indicating abrupt change in physical properties; abrupt change in AML amplitude; presence of 2 AML events that overlap by >400 m. Further discussion of imaging limitations and uncertainties in interpretation of AML segmentation is included in Supplementary Notes.

Erupted volume of 2005/2006 lavas. Along-axis variations in volume of the 2005–2006 lavas are calculated within 300 m bins oriented perpendicular to the axis using the mapped area of the lava flow from ref. 12 and assuming a uniform 1.5 m flow thickness.

Data sources. MCS data used in this study are available through the Marine Geoscience Data System (http://www.marine-geo.org/tools/search/entry.php?id=MGL0812). Bathymetric data are from the GMRT Synthesis (http://www.marine-geo.org/tools/maps_grids.php). Hydrothermal vent locations are from the Ridge2000 Data Portal (http://www.marine-geo.org/portals/ridge2000/vents.php?feature_id=EPR).

Geochemical data are from refs 1,3,13,14,20 (available from PetDB, www.petdb.org) and the 'Basalt Glasses from the EPR' compilation of M. Perfit available through http://www.earthchem.org/library/search. See refs 3,13 for discussion of analytical methods. Samples are filtered for those located within ±500 m of the axis.

Received 21 November 2012; accepted 1 August 2013; published online 15 September 2013

References

1. Langmuir, C. H., Bender, J. F. & Batiza, R. Petrological and tectonic segmentation of the East Pacific Rise, 5° 30′–14° 30′ N. *Nature* **322,** 422–429 (1986).
2. Macdonald, K. C. *et al.* A new view of the mid-ocean ridge from the behaviour of ridge-axis discontinuities. *Nature* **335,** 217–225 (1988).
3. Smith, M. C. *et al.* Magmatic processes and segmentation at a fast spreading mid-ocean ridge: Detailed investigation of an axial discontinuity on the East Pacific Rise crest at 9° 37′ N. *Geochem. Geophys. Geosyst.* **2,** 1040 (2001).
4. White, S. M. *et al.* Correlation between volcanic and tectonic segmentation of fast-spreading ridges: Evidence from volcanic structures and lava flow morphology on the East Pacific Rise at 9°–10° N. *J. Geophys. Res.* **107,** 2173 (2002).
5. Toomey, D. R., Jousselin, D., Dunn, R. A., Wilcock, W. S. D. & Detrick, R. S. Skew of mantle upwelling beneath the East Pacific Rise governs segmentation. *Nature* **446,** 409–414 (2007).
6. Haymon, R. M. *et al.* Hydrothermal vent distribution along the East Pacific Rise crest (9° 09′–9° 54′ N) and its relationship to magmatic and tectonic processes on fast spreading Mid-Ocean Ridges. *Earth Planet. Sci. Lett.* **104,** 513–534 (1991).
7. Fornari, D. J., Haymon, R. M., Perfit, M. R., Gregg, T. K. P. & Edwards, M. H. Axial summit trough of the East Pacific Rise 9°–10° N: Geological characteristics and evolution of the axial zone on fast spreading mid-ocean ridges. *J. Geophys. Res.* **103,** 9827–9855 (1998).
8. White, S. M., Haymon, R. M. & Carbotte, S. A new view of ridge segmentation and near-axis volcanism at the East Pacific Rise, 8°–12° N, from EM300 multibeam bathymetry. *Geochem. Geophys. Geosyst.* **7,** Q12O05 (2006).
9. Dunn, R. A., Toomey, D. R. & Solomon, S. C. Three-dimensional seismic structure and physical properties of the crust and shallow mantle beneath the East Pacific Rise at 9° 30′ N. *J. Geophys. Res.* **105,** 23537–23555 (2000).
10. Haymon, R. M. *et al.* Volcanic eruption of the mid-ocean ridge along the East Pacific Rise crest at 9° 45–52′ N: Direct submersible observations of seafloor phenomena associated with an eruption event in April, 1991. *Earth Planet. Sci. Lett.* **119,** 85–101 (1993).
11. Tolstoy, M. *et al.* A sea-floor spreading event captured by seismometers. *Science* **314,** 1920–1922 (2006).
12. Soule, S. A., Fornari, D. J., Perfit, M. R. & Rubin, K. H. New insights into mid-ocean ridge volcanic processes from the 2005–2006 eruption of the East Pacific Rise, 9° 46′ N–9° 56′ N. *Geology* **35,** 1079–1082 (2007).
13. Goss, A. R. *et al.* Geochemistry of lavas from the 2005–2006 eruption at the East Pacific Rise, 9° 46′ N–9° 56′ N: Implications for ridge crest plumbing and decadal changes in magma chamber compositions. *Geochem. Geophys. Geosyst.* **11,** Q05T09 (2010).
14. Perfit, M. *et al.* Lava geochemistry as a probe into crustal formation at the East Pacific Rise. *Oceanography* **25,** 21–24 (2012).
15. Rubin, K. H. *et al.* Volcanic eruptions in the deep sea. *Oceanography* **25,** 142–157 (2012).
16. Soule, S. A., Escartín, J. & Fornari, D. J. A record of eruption and intrusion at a fast spreading ridge axis: Axial summit trough of the East Pacific Rise 9–10° N. *Geochem. Geophys. Geosyst.* **10,** Q10T07 (2009).

17. Kent, G. M., Harding, A. J. & Orcutt, J. A. Distribution of magma beneath the East Pacific Rise between the Clipperton transform and the 9° 17′ N deval from forward modeling of common depth point data. *J. Geophys. Res.* **98,** 13945–13969 (1993).
18. Carton, H. D. *et al*. Three-dimensional seismic reflection images of axial melt lens and seismic layer 2A between 9° 42′ N and 9° 57′ N on the East Pacific Rise. *EOS Trans. AGU abstr.* OS21C-1514 (2010).
19. Kent, G. M. *et al*. Evidence from three-dimensional seismic reflectivity images for enhanced melt supply beneath mid-ocean ridge discontinuities. *Nature* **406,** 614–618 (2000).
20. Sims, K. W. W. *et al*. Aberrant youth: Chemical and isotopic constraints on the origin of off-axis lavas from the East Pacific Rise, 9°–10° N. *Geochem. Geophys. Geosyst.* **4,** 8621 (2003).
21. Fundis, A. T., Soule, S. A., Fornari, D. J. & Perfit, M. R. Paving the seafloor: Volcanic emplacement processes during the 2005–2006 eruptions at the fast spreading East Pacific Rise, 9° 50′ N. *Geochem. Geophys. Geosyst.* **11,** Q08024 (2010).
22. Varga, R. J., Horst, A. J., Gee, J. S. & Karson, J. A. Direct evidence from anisotropy of magnetic susceptibility for lateral melt migration at superfast spreading centers. *Geochem. Geophys. Geosyst.* **9,** Q08008 (2008).
23. Stewart, M. A., Karson, J. A. & Klein, E. M. Four-dimensional upper crustal construction at fast-spreading mid-ocean ridges: A perspective from an upper crustal cross-section at the Hess Deep Rift. *J. Volcanol. Geotherm. Res.* **144,** 287–309 (2005).
24. Bergmanis, E. C., Sinton, J. & Rubin, K. H. Recent eruptive history and magma reservoir dynamics on the southern East Pacific Rise at 17° 30′ S. *Geochem. Geophys. Geosyst.* **10,** Q12O06 (2007).
25. Kelemen, P. B., Koga, K. & Shimizu, N. Geochemistry of gabbro sills in the crust-mantle transition zone of the Oman ophiolite: Implications for the origin of the oceanic lower crust. *Earth Planet Sci. Lett.* **146,** 475–488 (1997).
26. Natland, J. H. & Dick, H. J. B. Paired melt lenses at the East Pacific Rise and the pattern of melt flow through the gabbroic layer at a fast-spreading ridge. *Lithos* **112,** 73–86 (2009).
27. Mutter, J. C. *et al*. Seismic images of active magma systems beneath the East Pacific Rise between 17° 05′ and 17° 35′ S. *Science* **21,** 391–395 (1995).
28. Coogan, L. A., Mitchell, N. C. & O'Hara, M. J. Roof assimilation at fast-spreading ridges: An investigation combining geophysical, geochemical and field evidence. *J. Geophys. Res.* **108,** 2002 (2003).
29. Fontaine, F. J., Olive, J-A., Cannat, M., Escartín, J. & Perol, T. Hydrothermally-induced melt lens cooling and segmentation along the axis of fast- and intermediate-spreading centers. *Geophys. Res. Lett.* **38,** L14307 (2011).
30. Von Damm, K. L. in *Mid-Ocean Ridges: Hydrothermal Interactions Between the Lithosphere and Ocean* (ed. German, C. R.) 285–304 (AGU Geophys. Mono., Vol. 148, American Geophysical Union, 2004).

Acknowledgements

We thank Captain M. Landow, crew, and technical staff led by R. Steinhaus for the success of RV *M.G. Langseth* cruise MGL0812. We thank I. Grevemeyer for comments, R. Waters for assistance with the geochemical data, and K. C. Macdonald, R. M. Haymon and R. Buck for helpful discussions. This research was financially supported by NSF OCE0327872 to S.M.C. and J.C.M., OCE0327885 to J.P.C., and OCE0138088 to M.R.P.

Author contributions

All authors (except M.R.P. and S.H.) participated in the MCS field experiment. M.M. carried out the MCS data processing, S.M.C. and M.M. interpreted the data. M.R.P. contributed geochemical data and interpretation. S.M.C. wrote the paper with contributions from all co-authors.

Additional information

Supplementary information is available in the online version of the paper. Reprints and permissions information is available online at www.nature.com/reprints. Correspondence and requests for materials should be addressed to S.M.C.

Competing financial interests

The authors declare no competing financial interests.

nature geoscience
SUPPLEMENTARY INFORMATION
DOI: 10.1038/NGEO1933

Fine-scale segmentation of the crustal magma reservoir beneath the East Pacific Rise

Supplementary Notes

Uncertainties in interpretation of AML structure.

A number of factors need to be considered in the evaluation of AML segmentation and depth variations beneath the axial zone derived from our along-axis seismic data, including imaging limitations inherent with the 2D processing, and uncertainties in depth estimates due to departure from the constant velocities assumed for depth conversion.

1. AML depth: Imaging limitations

Images of the AML event obtained from the axially-centered seismic profiles are subject to contamination from "side-swipe" energy arising from features located outside of the imaging plane or from sampling of diffractive energy from the AML which can not be properly migrated given the limited across-axis footprint of the along-axis seismic data. These factors can lead to two-way travel time (twtt) variations in the AML image that could be misinterpreted as true structure. These limitations are alleviated with full 3D surveys where side-swipe events and diffractions can be back projected/collapsed to their true subsurface position. In our study, the potential contribution of these factors can be evaluated for the region of 3D coverage from ~9°37' to 40'N and 9°42' to 9°57'N. Comparison of the twtt of the AML identified from the along-axis 2D processed data set with that identified along a coincident line extracted from the migrated 3D data volume [Carton et al., 2010] shows the two data sets agree well with average mismatch in twtt to the AML of only 10 msec. Prior regional-scale seismic studies from 8°50 to 9°55'N [Kent et al., 1993a and b] indicate that the AML is narrower within the area of our 3D coverage (500-700 m) than elsewhere along the ridge (1 to 4 km), and the potential for sampling diffractive energy from this body should be higher for the region where our 3D coverage is located. The good agreement between the axial zone AML image obtained from the 2D and 3D datasets in this region of narrow AML, lends confidence to the interpretation of AML structure elsewhere where a wider AML body is inferred and impact of imaging limitations associated with the 2D acquisition should be less.

2. AML depth: Variable crustal velocities

The axial seismic sections reveal an undulating AML horizon with abrupt steps in twtt at many AML disruptions (few 10's up to 150 msec) as well as gradual variations in AML twtt within lens segments (Supplementary Figure S3). In this study, the depth to the AML reflection (Figure 2) is calculated from twtt to the layer 2A and AML events and assuming constant velocities for layer 2A and 2B. However, velocities within these upper crustal layers may vary significantly along-axis from the constant velocities assumed, contributing to the undulations in the AML event in the traveltime sections. A number of factors may give rise to spatial gradients in upper crustal seismic velocities including cracking and alteration associated with hydrothermal flow, changes in rock composition, and perhaps thermal perturbations associated with dike intrusions. At present, information on upper crustal velocities within the region is only available at a few locations and along-axis variations are unknown [Vera et al., 1990; Christeson et al., 1996]. To gain perspective on the potential contribution of variable velocities to AML traveltimes, we consider a range of average velocities for layer 2A and 2B reported in prior studies of young fast-intermediate spread crust as the potential range present within our study area (2200-2500 m/s and 5100-5500 m/s, from Vera et al., 1990; Harding et al., 1993; Hussenoeder et al., 2000; Canales et al., 2005; Baran et al., 2010). This range of velocities can account for variations in AML twtt of up 40 msec for a 200 m thick layer 2A and 1400 m thick layer 2B, much less than the total variation (450 msec) observed in the study area. Furthermore, to account for the abrupt steps in AML traveltimes observed at many magma lens disruptions, very steep spatial gradients in crustal velocities would be required that are unlikely. However, plausible variations in seismic velocities could contribute to the more gradual variations in AML traveltimes within individual magma lens segments linked to, for example, along-axis hydrothermal flow. If regions of hydrothermal downflow and enhanced cracking are preferentially located at lens discontinuities, as has been proposed [Tolstoy et al., 2008; Fontaine et al., 2011], zones of lower seismic velocity may develop in the upper crust contributing to the longer traveltimes near AML disruptions and the dome-shaped AML profile of many magma lens segments. However, true deepening of the magma lens near segment ends is also predicted with along-axis hydrothermal flow [e.g. Fontaine et al., 2011] and we expect that this process will give rise to both spatial gradients in upper crustal velocities and true variations in the depth of the AML. Future studies of upper crustal velocities using refracted arrivals recorded with the 6-km-long streamers used in our study will be needed to further refine AML depth and structure from the axial seismic profiles.

3. AML Segmentation: Imaging Limitations

Artifacts associated with side-scattered energy and diffractions as described above can also lead to disruptions in the AML image that are not due to real structure of the axial magma body. Furthermore, complexities in the plan view shape of the AML relative to the axial eruption zone and location of our 2D profiles may complicate interpretation of magma body segmentation. In this study, the primary segmentation of the magma body is interpreted with high confidence in the region of 3D coverage where diffractions are collapsed and the plan view geometry of the magma body is properly imaged. Outside this region, we can not rule out the possibility that AML disruptions imaged beneath the axial eruptive zone reflect other complexity in AML geometry. For example, our seismic profiles could sample the more discontinuous edges of a magma lens segment in places, leading to disruptions in the AML image that do not reflect the primary segmentation of the magma body. Given the criteria adopted in this study for identification of AML disruptions (see Methods), we also expect that AML segmentation may be under identified in some places, for example where local twtt maxima in the AML reflection are observed and the reflection amplitude weakens (e.g. 8°42'N, 8°47'N, 9°18'N, Figs. S2, S3). Future 3D MCS surveys will be needed to further refine the location of AML segmentation identified here.

References

Baran, J., S. M. Carbotte, J. R. Cochran & Nedimović, M. R. Evolution of upper crustal seismic properties along the South East Indian Ridge within young crust (0-550 ka) and variation with axial morphology. *G-cubed* **11**, Q02001 (2010).

Canales, J. P., R. S. Detrick, S. M. Carbotte, G. M. Kent, J. B. Diebold, A. J. Harding, J. Babcock, M. R. Nedimović, & van Ark, E. Upper crustal structure and axial topography at intermediate-spreading ridges: seismic constraints from the Southern Juan de Fuca Ridge. *J. Geophys. Res.* **110**, (2005).

Canales, J. P., H. Carton, S. M. Carbotte, J. C. Mutter, M. R. Nedimović, M. Xu, O. Aghaei, M. Marjanović, & Newman, K. Network of off-axis melt bodies at the East Pacific Rise. *Nature Geoscience*, doi:10.1038/NGEO1377 (2012).

Carton, H.D., Carbotte, S.M., Mutter, J.C., Canales, J., Nedimović, M.R., Aghaei, O., Marjanović, M., & Newman, K.R., Three-dimensional seismic reflection images of axial melt lens and seismic layer 2A between 9°42’N and 9°57’N on the East Pacific Rise. *EOS Trans. Abstract* OS21C-1514 (2010).

Christeson, G.L., Kent, G.M., Purdy, G.M. & Detrick, R.S. Extrusive thickness variability at the East Pacific Rise, 9°-10°N: Constraints from seismic techniques. *J. Geophys. Res*. **101**, 2859-2873 (1996).

Kent, G. M., Harding, A. J., & Orcutt, J.A. Distribution of magma beneath the East Pacific Rise between the Clipperton transform and the 9°17'N deval from forward modeling of common depth point data. *J. Geophys. Res.* **98**, 13,945-13,969 (1993a).

Kent, G.M., Harding, A.J., & Orcutt, J.A. Distribution of magma beneath the East Pacific Rise near the 9˚03’N overlapping spreading center from forward modeling of common depth point data. *J. Geophys. Res.* **98**, 13,971-13,995 (1993b).

Fontaine, F. J., J.-A. Olive, M. Cannat, J. Escartín, & Perol, T. Hydrothermally-induced melt lens cooling and segmentation along the axis of fast- and intermediate-spreading centers. *Geophys. Res. Lett.* **38**, L14307 (2011).

Harding, A.J., G.M. Kent & Orcutt, J.A. A multichannel seismic investigation of upper crustal structure at 9^0 N on the East Pacific Rise: implications for crustal accretion. *J. Geophys. Res. 98*, 13,925–13,944 (1993).

Hussenoeder, S. A., Detrick, R. S., Kent, G. M., Schouten, H., & Harding, A. Fine-scale seismic structure of young upper crust at 17◦ 20′ S on the fast spreading East Pacific Rise. *J. Geophys. Res*. **107**, (2002).

Mutter, J. C. Carbotte, S.M., Nedimovic, M., Canales, J.P., & Carton, H. Seismic imaging in three dimensions on the East Pacific Rise. *Eos Trans. AGU* **90**, 374-375 (2009).

Ryan, W.B.F., Carbotte, S.M., Coplan, J.O., O’Hara, S., Melkonian, A., Arko, R., Weissel, R.A., Ferrini, V., Goodwillie, A., Nitsche, F., Bonczkowski, J., & Zemsky, R. The Global Multi-Resolution Topography Synthesis. *Geochem. Geophys. Geosyst.* **10** (2009).

Tolstoy, M., Waldhauser, F. , Bohnenstiehl, D. R., Weekly, R. T. & Kim, W.-Y. Seismic identification of along-axis hydrothermal flow on the East Pacific Rise. *Nature* **451**, 181-184 (2008).

Vera, E. E. *et al.*, The structure of 0- to 0.2-m.y.-old oceanic crust at 9°N on the East Pacific Rise from expanded spread profiles. *J. Geophys. Res.* **95**, 15,529-15,556 (1990).

White, S. M., R. M. Haymon, & Carbotte, S. A new view of ridge segmentation and near-axis volcanism at the East Pacific Rise, 8°-12°N, from EM300 multibeam bathymetry, *Geochem. Geophys. Geosyst.,* **7***,* Q12O05 (2006).

Supplementary Figures

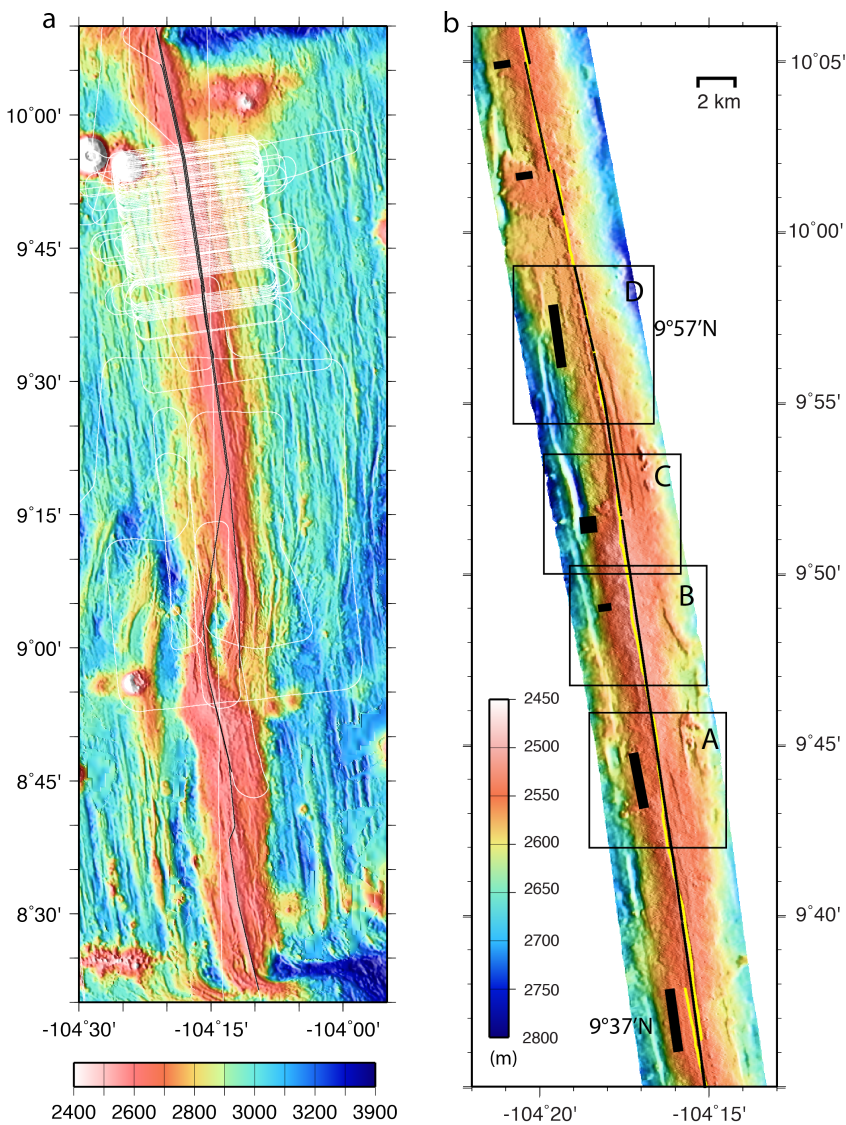

Supplementary Figure S1. Bathymetry and track coverage for study area. Left Panel: Seismic track coverage from R/V *M.G. Langseth* expedition MGL0812 (white lines) includes a suite of ridge perpendicular lines acquired for 3D imaging and a series of along-axis profiles from 8°20-10°10'N (black). Full details on acquisition parameters and survey layout are given in Mutter et al. [2009] and Canales et al. [2012]. Bathymetric data are from the GMRT synthesis [Ryan et al., 2009]. Right Panel: Location of composite seismic profile (black line) compared with axial eruptive zone (yellow line, see also Fig. 1A) superimposed on high-resolution EM300 bathymetry data from White et al. [2006]. Filled black rectangles indicate latitude range of small 3rd (central latitude labelled) and 4th order discontinuities of axial eruptive zone. Close-up bathymetry maps and seismic sections for several axial discontinuities are shown in Fig. S2 (open black boxes A-D).

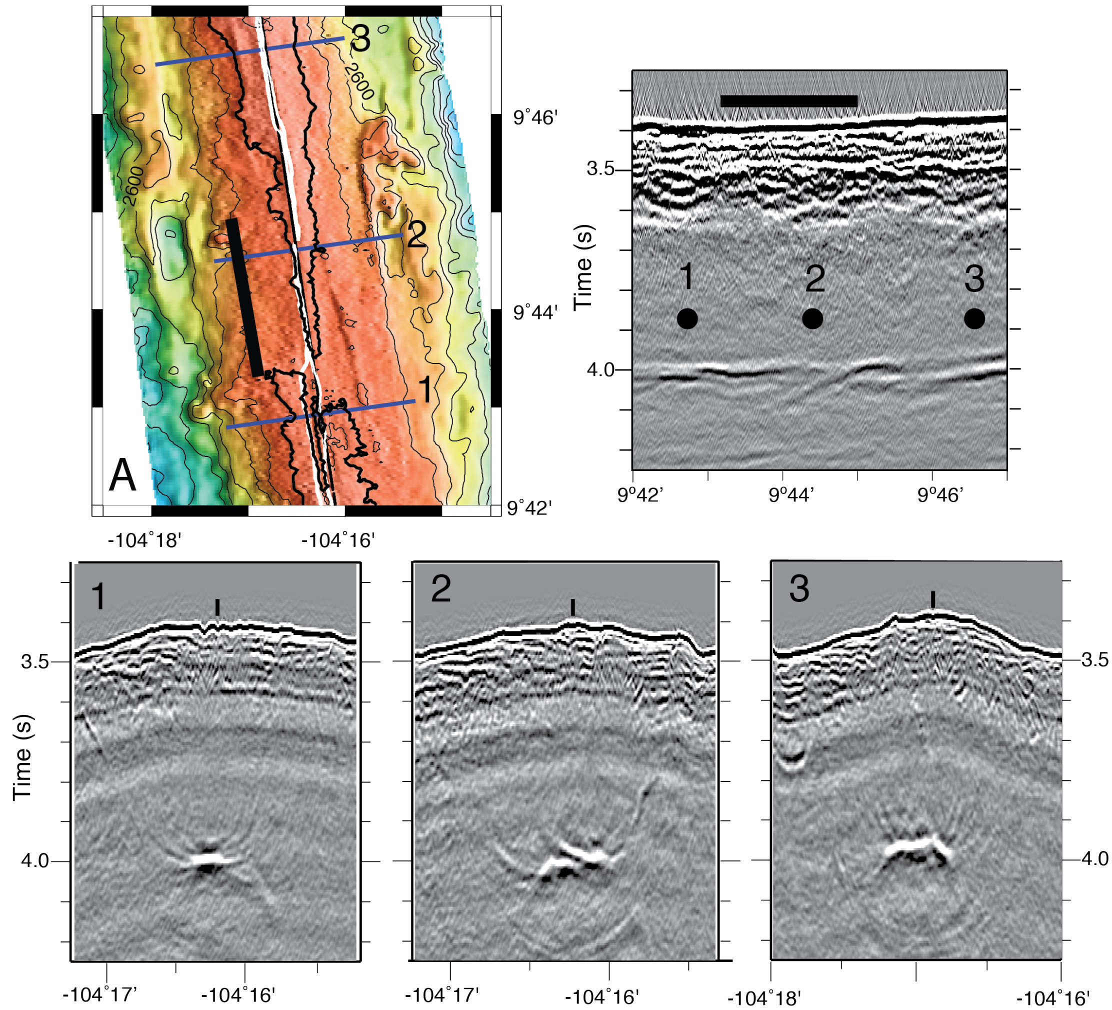

Supplementary Figure S2a. Bathymetric and seismic data illustrating the co-located discontinuity in the axial eruptive zone and underlying magma lens centered at ~ 9°44’N. **Top left**: Close up of high-resolution bathymetry from Fig. S1b (box A). Discontinuity zone (highlighted with black rectangle) is identified from right step in axial summit trough (AST, white line) picked from near bottom side-scan sonar data (from Soule et al. [2007]) and change from narrow (north) to wide AST (south). Beyond the AST, the discontinuity is evident in narrowing and pinch out of the crest of the axial high (bold black contour) in the north and change to broader crest (south). Location of axis-centered seismic profile and 3 profiles through 3D seismic volume are shown in black and blue line respectively. **Top right**: Axis-centered seismic profile showing discontinuity in AML reflection at ~9°44.2’-44.8’N evident as a zone of two overlapping melt lenses, one dipping beneath the other. Numbered black dots show locations of the cross-axis profiles extracted from the 3D volume shown below. **Bottom**: Inlines from 3D volume (layer 2A event not shown). Processing sequence similar to that of Canales et al. [2012] comprised flexible binning, CMP stacking and two-pass Kirchhoff post-stack time migration. Vertical black tick marks at the seafloor indicate location of the AST. Profile 2 crosses the discontinuity zone and shows two discrete overlapping magma lenses; a narrower and deeper magma lens is present to the south of the discontinuity (profile 1) than to the north (profile 3).

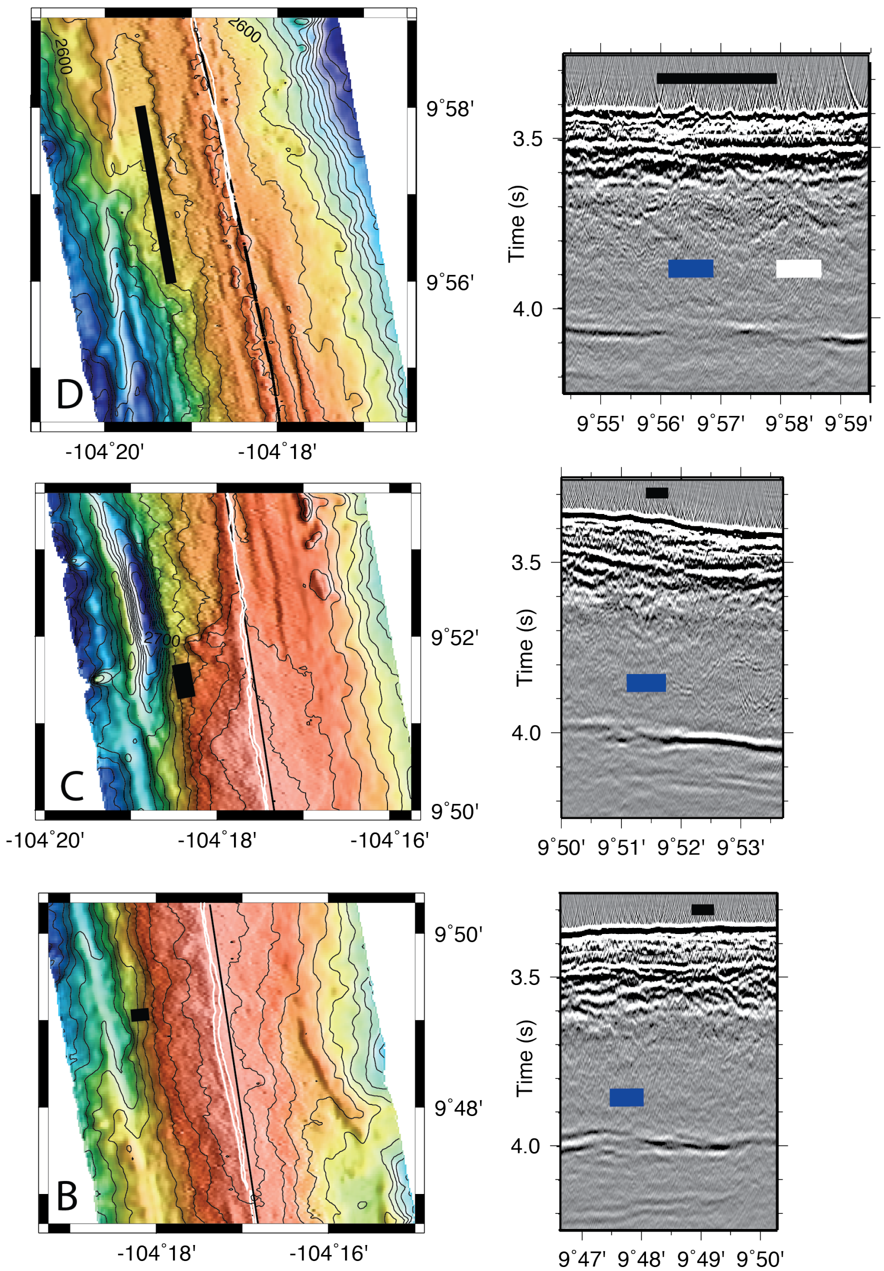

Supplementary Figure S2b. Bathymetric and seismic data illustrating nature of seafloor discontinuities and underlying magma lens disruptions. Left panels: Close up of high-resolution bathymetry from Fig. S1b centered on discontinuities at 9°48'N (box B), 9 51.5'N (box C) and 9°57'N (box D) also showing AST (white line) where present and location of axis-centered seismic profile (black line). Right panels: seismic section showing seafloor, layer 2A, and AML reflections. Latitude extent of bathymetric discontinuities shown above seafloor reflection in thick black line; AML discontinuities in white and blue boxes (blue indicates discontinuities identified from 3D volume). 9°48'N discontinuity (B) corresponds with right bend in AST and right jog in edge of axial high. 9°51.5'N discontinuity (C) corresponds with transition from broad shallow axial high with well-defined AST (south) to deeper axial high with axial pillow ridges and faults transecting the ridge crest. 9°57'N discontinuity (D) corresponds with change from axial zone of pillow ridges and faults across ridge crest (south) to zone of discontinuous pillow mounds and depressions at crest. Beyond axial zone the discontinuity is evident as left stepping jog/bend in axial high.

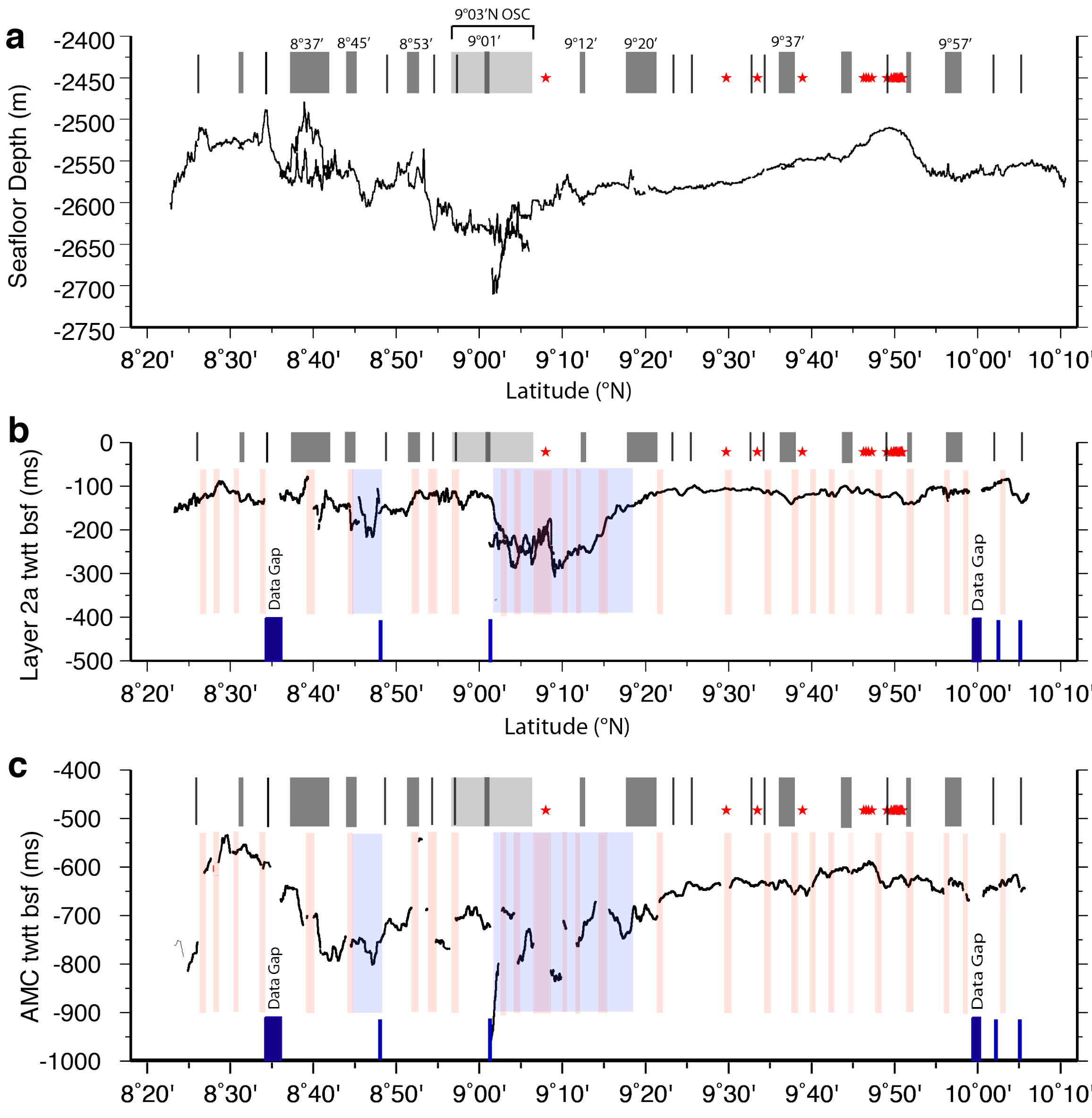

Supplementary Figure S3. **a**) Seafloor depth measured along the AST or crest of axial pillow ridges that define the present-day zone of primary eruptive fissures and hydrothermal venting along the EPR. Depth is digitized from EM300 high-resolution bathymetry of White et al. [2006]. **b**) Two-way travel time to Layer 2A event below seafloor (bsf) digitized from composite along-axis profile. **c**) Two-way travel time to AML reflection event below seafloor (bsf) digitized from composite along-axis profile.

For all 3 panels bathymetric discontinuities of the axial zone [modified from White et al., 2006] are indicated with vertical grey lines and grey shaded boxes (showing the along-axis extent of broader discontinuity zones composed of overlapping, offset pillow ridges or axial summit troughs). All 3rd order tectonic discontinuities are labeled in part **a** with central latitude of these offset zones. Latitude range of 9°03'N OSC shown with light grey bar. Red stars show location of hydrothermal vents (Von Damm, 2004). For panels **b** and **c** vertical light red shaded bars indicate locations of magma lens discontinuities. Light blue shaded regions indicate where seismic profile is located more than 300 m from the axial zone and/or where modern axis is difficult to identify; uncertainty in interpretation of axial AML segmentation is greater in these regions. Short blue lines/bars at bottom of figure indicate seismic data gaps and location of joins between seismic lines forming the composite axial profile.

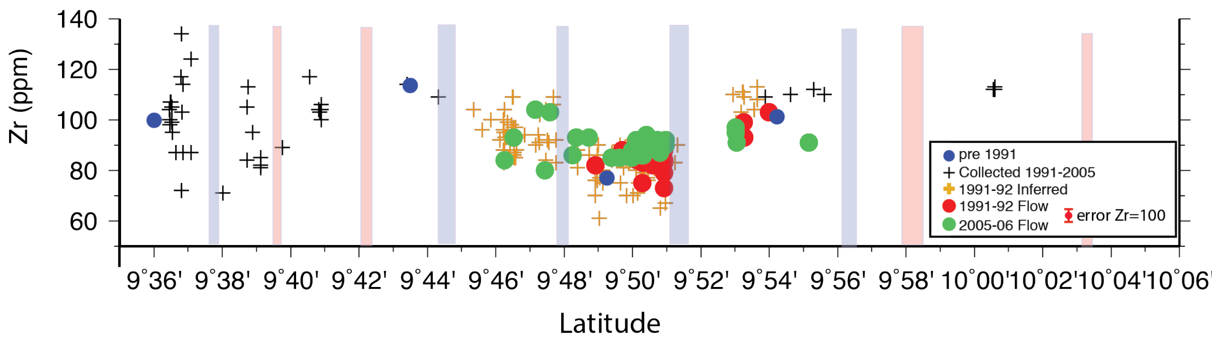

Figure S4. Zr composition of seafloor lavas located within 500 m of the axis color coded for date of eruption as in Fig 1c. Crosses correspond with samples collected between 1991 and 2005; orange crosses are inferred to be 1991-92 lavas. Zr is measured by ICP-MS or XRF on handpicked basalt glasses. Analytic errors on natural glasses are better than ±2 relative% for ICP-MS analyses and better than ± 5% for XRF analyses. Error bar shown is ±5 ppm for a value of 100 ppm. Vertical red and blue bars mark magma lens disruptions from Fig. 1b (blue indicates disruptions resolved in 3D dataset). Zr compositions are an indicator of extent of fractionation (all samples are N-MORB) and inversely correlated with MgO which is a proxy for magma temperature. Although sample density for Zr is less than for MgO, a similar spatial distribution of limited range in Zr coincident with the magma lens segments is apparent. See Methods for data sources.